

Ion and electron acoustic bursts during anti-parallel magnetic reconnection driven by lasers

Received: 25 February 2022

Accepted: 31 January 2023

Published online: 2 March 2023

 Check for updates

Shu Zhang¹✉, Abraham Chien¹, Lan Gao², Hantao Ji^{1,2}✉, Eric G. Blackman^{3,4}, Russ Follett⁴, Dustin H. Froula⁴, Joseph Katz⁴, Chikang Li⁵, Andrew Birkel⁵, Richard Petrasso⁵, John Moody⁶ & Hui Chen⁶

Magnetic reconnection converts magnetic energy into thermal and kinetic energy in plasma. Among the numerous candidate mechanisms, ion acoustic instabilities driven by the relative drift between ions and electrons (or equivalently, electric current) have been suggested to play a critical role in dissipating magnetic energy in collisionless plasmas. However, their existence and effectiveness during reconnection have not been well understood due to ion Landau damping and difficulties in resolving the Debye length scale in the laboratory. Here we report a sudden onset of ion acoustic bursts measured by collective Thomson scattering in the exhaust of anti-parallel magnetically driven reconnection using high-power lasers. The ion acoustic bursts are followed by electron acoustic bursts with electron heating and bulk acceleration. We reproduce these observations with one- and two-dimensional particle-in-cell simulations in which an electron outflow jet drives ion acoustic instabilities, forming double layers. These layers induce electron two-stream instabilities that generate electron acoustic bursts and energize electrons. Our results demonstrate the importance of ion and electron acoustic dynamics during reconnection when ion Landau damping is ineffective, a condition applicable to a range of astrophysical plasmas including near-Earth space, stellar flares and black hole accretion engines.

Magnetic reconnection is a fundamental physical process through which energy is rapidly converted from magnetic field to plasma by alternating magnetic topology^{1,2}. Magnetic reconnection has been considered as a key energy release mechanism during solar and stellar flares³, in Earth's magnetosphere⁴ and during energetic phenomena in the distant Universe such as the black hole's accretion disc^{5,6}. It has been a long-standing challenge to identify the underlying kinetic

mechanisms for efficient dissipation required for topological change as well as energy conversion to explain the observed fast reconnection in nearly collisionless plasmas in space and astrophysics. There has been progress in understanding and confirming two-dimensional (2D) kinetic mechanisms often represented by non-gyrotropic pressure tensor⁷⁻¹⁰ in electron diffusion regions where field lines break and reconnect. Beyond these 2D laminar processes, however, the kinetic

¹Department of Astrophysical Sciences, Princeton University, Princeton, NJ, USA. ²Princeton Plasma Physics Laboratory, Princeton University, Princeton, NJ, USA. ³Department of Physics and Astronomy, University of Rochester, Rochester, NY, USA. ⁴Laboratory for Laser Energetics, University of Rochester, Rochester, NY, USA. ⁵Plasma Science and Fusion Center, Massachusetts Institute of Technology, Cambridge, MA, USA. ⁶Lawrence Livermore National Laboratory, Livermore, CA, USA. ✉e-mail: shuzhang@princeton.edu; hji@pppl.gov

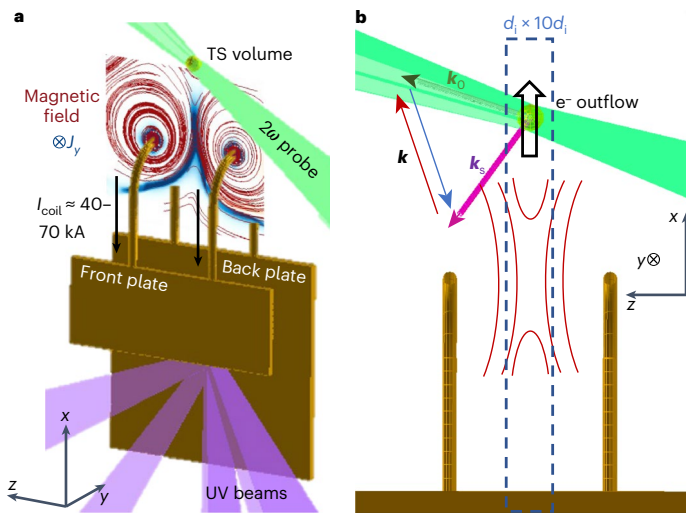


Fig. 1 | Experimental setup and Thomson scattering diagnostics. **a**, Six UV beams (purple) are used to irradiate the back plate of the capacitor, driving current in the coils with $I_{\text{coil}} \approx 40\text{--}70$ kA. The black arrows mark the current directions in the coils. FLASH MHD simulation results are overlapped with the target to show the structure of the magnetic field (red lines) and the out-of-plane current density (blue) in the y direction. A 2ω (527 nm) Thomson scattering beam (green) probes the reconnection exhaust region, $600\ \mu\text{m}$ above the centre point between the top of the coils. The scattered light in a volume $60 \times 60 \times 50\ \mu\text{m}^3$ is collected by an $f/10$ reflective collection system. **b**, Face-on view of the reconnection region. The two vertical brown lines are the coils in **a**. Here \mathbf{k}_0 and \mathbf{k}_s are the wavevectors of the probe beam and collected scattered light, respectively. The red and blue arrows indicate the wavevectors (\mathbf{k}) of the waves in plasma resonant with the probe and scattered light. The red arrow is for the wave generating redshifted scattered light, and the blue arrow is for the wave generating blueshifted scattered light. These \mathbf{k} wavevectors are in the x - z plane and 17° off the outflow direction. The blue dashed box indicates a $d_i \times 10d_i = 180\ \mu\text{m} \times 1,800\ \mu\text{m}$ region, in which the ion skin depth $d_i = c/\omega_{\text{pi}}$, where ω_{pi} is the Cu^{18+} -ion plasma frequency. The red lines illustrate the magnetic-field lines, and the hollow arrow is the direction of electron outflow jet measured by Thomson scattering in this experiment.

dissipation mechanisms generally operating in three dimensions are still much less understood^{11,12} within or near diffusion regions and separatrices¹³ that feature strong spatial gradients and streaming. They include various plasma waves or instabilities, such as whistler waves^{14,15}, Buneman instabilities^{16–18}, lower hybrid drift waves^{19–26} (due to cross-field gradient²⁷ or cross-field drift²⁸), drift kink²⁹ or kinetic Kelvin–Helmholtz³⁰ instabilities.

Among these three-dimensional (3D) candidate dissipation mechanisms, unstable ion acoustic waves (IAWs)^{31–34} driven by a relative drift between electrons and ions (or equivalently, electric current) have attracted considerable interest as potential sources for enhanced resistivity or viscosity that are often used within fluid descriptions as a local, current-dependent anomalous resistivity required for the sustained Petschek model of fast reconnection^{35–40}. Despite early pioneering laboratory detection⁴¹, however, the importance of IAWs for magnetic reconnection has been quickly dismissed due to the widely observed high ion temperature ($T_i/Z \gg T_e$) in space and in the laboratory where IAWs are strongly stabilized by ion Landau damping. Technical difficulties in the laboratory in measuring plasma waves in short wavelengths on the order of the Debye length have also prevented progress in identifying IAWs and understanding their detailed properties and role in magnetic reconnection.

In this Article, we present a laboratory platform where reconnection is magnetically driven at low β by laser-powered capacitor coils⁴² in plasmas with high mean ion charge (Z), namely, $T_i/Z \ll T_e$, where T_i is the ion temperature and T_e is the electron temperature. The sudden

onset of bursts of IAWs is successfully measured in the exhaust region by collective Thomson scattering diagnostics. The IAWs are followed by bursts of electron acoustic waves (EAWs) with electron heating and electron bulk acceleration. The corresponding particle-in-cell (PIC) simulations in one-dimensional (1D) and 2D scenarios show that IAWs are destabilized by an electron exhaust jet where the relative drift between ions and electrons is large. IAWs grow rapidly to form electrostatic double layers, which, in turn, accelerate electrons to drive two-stream instability generating bursts of EAWs as electrons are heated. Our results demonstrate the importance of ion and electron acoustic dynamics causing bursty energy dissipation during magnetic reconnection when ion Landau damping is ineffective. Implications for the reconnection process in magnetically dominated plasmas during stellar flares and accretion onto black holes are discussed.

Reconnection platform with laser-driven capacitor coils

The presented experiments were performed at the OMEGA laser facility, Laboratory for Laser Energetics, University of Rochester⁴³. The experimental platform is shown in Fig. 1. The capacitor-coil target is made of a $50\text{-}\mu\text{m}$ -thick Cu foil laser cut to the shape of two plates connected by two wires. The wires, separated by $600\ \mu\text{m}$, are bent to $600\ \mu\text{m}$ diameter half-circle coils and $500\ \mu\text{m}$ straight legs. The target pictures are presented in Supplementary Fig. 4. Six beams of $500\ \text{J}$ ns ultraviolet (UV) ($\lambda = 351\ \text{nm}$) lasers are focused on the centre of the capacitor's back plate to drive an $40\text{--}70$ kA current in the coils forming an anti-parallel magnetic field. The laser-generated plasmas diffuse into the region between the coils, and the X-rays and current also heat the coils generating the plasmas. The plasma between the coils is magnetized by the coil-driven anti-parallel magnetic field, forming a reconnection current sheet.

The magnetic field generated by the capacitor-coil targets is measured using proton radiography⁴⁴, similar to our previous experiments^{42,45–47}. The upstream magnetic-field strength is $23\text{--}40$ T at 6 ns after the lasers' onset. The proton radiographs also show that the reconnection current sheet exists. The radiographs and analyses are presented in the Supplementary Information. To further quantify the reconnection conditions, we have conducted radiative and non-ideal magnetohydrodynamic (rad-MHD) simulations using the FLASH code⁴⁸ to simulate the plasma diffusing from the capacitor plates and plasma emerging from the heated coils due to ohmic heating and X-ray radiation. Supplementary Information details the setup of the non-ideal rad-MHD simulation. The simulated magnetic-field lines and current density at 3 ns, overlapped on the target in Fig. 1a, show that a reconnection current sheet is formed between the coils. This reconnection current sheet lasts until 10 ns (Supplementary Fig. 2). The synthetic proton radiographs (Supplementary Fig. 3d,e) have a current-sheet-induced central flask-like feature, consistent with the experimental one (Supplementary Fig. 3a).

An approach to study kinetic instabilities in reconnection is provided by combining a laser-driven capacitor-coil reconnection platform with collective Thomson scattering. Collective Thomson scattering diagnoses the spectrum of the density fluctuations in plasmas, which may be due to the microturbulence induced by kinetic instabilities^{49–51}. It can also diagnose the Stokes and anti-Stokes scattering of natural resonances in plasmas, such as IAWs and electron plasma waves (EPWs). Since the plasma parameters determine the spectrum of the IAW- and EPW-induced scattering, Thomson scattering is frequently used to diagnose the plasma's density, temperature, mean ion charge, flow speed, electron–ion relative drift and non-Maxwellian distribution^{52–58}.

In this experiment, we recorded the Thomson scattering spectrogram of a probe laser ($\lambda = 527\ \text{nm}$, $150\ \text{J}$ energy, $3.7\ \text{ns}$ square pulse, $60\ \mu\text{m}$ spot size) focused at $600\ \mu\text{m}$ ($\sim 3d_i$) above the centre between the top of the coils (reconnection x line) (Fig. 1). As shown in Fig. 1b,

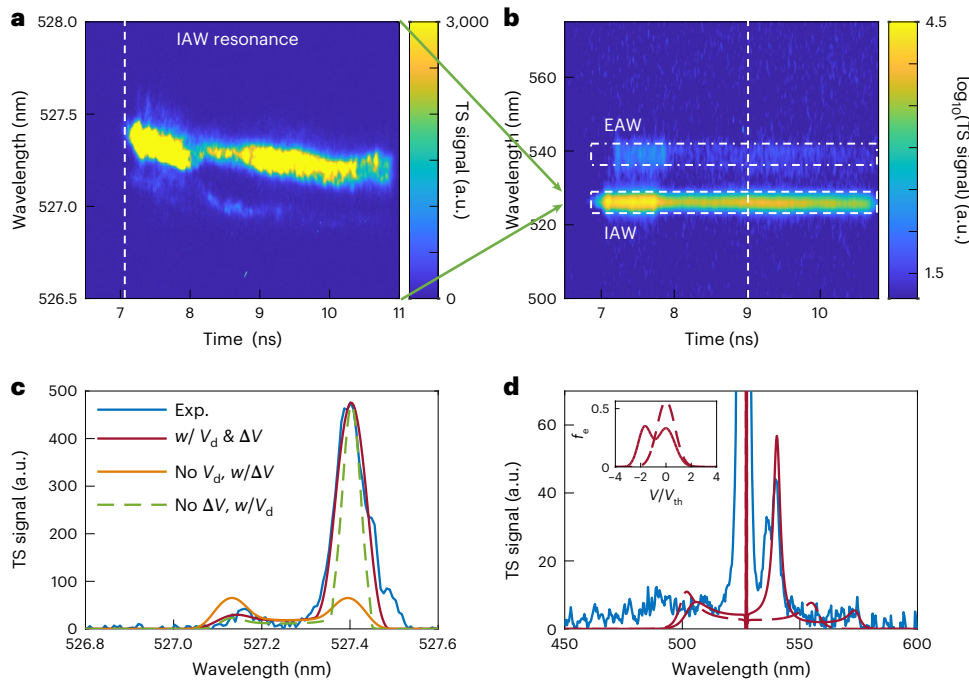


Fig. 2 | Thomson scattering data and analysis. **a, b**, Narrowband (IAW) (**a**) and broadband time-resolved (**b**) Thomson scattering (TS) at $t = 7\text{--}10$ ns. The IAW resonant peaks in **a** are highly asymmetric (grow from 10:1 to 100:1). **c**, Spectrum at 7.1 ns, before the IAW bursts (along the vertical dashed line in **a**), is shown as the blue line and compared with the synthetic TS spectra. The green dashed synthetic spectrum can reproduce the asymmetry of the IAW peaks, which is calculated with electrons streaming relative to ions with drift velocity $v_d = 0.17v_{th}$ (electron thermal velocity) along the k direction (Fig. 1b, red arrow). In addition to the electron drift, an inhomogeneous flow velocity with $\Delta v = 2 \times 10^4 \text{ m s}^{-1} \approx v_i$ (ion thermal velocity) in the scattering volume can broaden the IAW peak (red solid line) to match the experiment. A plasma without a drift but with

an inhomogeneous flow velocity would generate a symmetric IAW spectrum (orange line). The spectrogram in **b** is from the broadband spectrometer and shows both EAW resonance (dash-dotted line) and IAW feature (dashed line). **d**, Spectrum at 9 ns (vertical dashed line in **b**) is plotted as the blue line with a fitted synthetic spectrum (red solid line). A two-stream electron distribution (red solid line in the inset (f_e)) is needed to reproduce the strong EAW signal. The $-v$ direction is along the redshifted k (Fig. 1b). The velocity at the valley of the distribution ($-0.023c$) matches the EAW's phase velocity ($0.025c$). For reference, a Maxwellian distribution (dashed red line in the inset) would generate the red dashed spectrum.

the directions of the probe-light and scattered-light collector determine the wavevector \mathbf{k} of the measured density fluctuations or natural resonances since $\mathbf{k} = \mathbf{k}_0 - \mathbf{k}_s$ or $\mathbf{k} = \mathbf{k}_s - \mathbf{k}_0$. Here \mathbf{k} is in the direction 17° from the outflow direction ($+\mathbf{x}$) and $k \approx k_0 = 2\pi/527 \text{ nm}^{-1}$. To infer the exhaust plasma's parameters, we fit the synthetic Thomson scattering spectra to the measured spectra. The synthetic spectrum is calculated using equation (2). The least-squares fit suggests that the plasma in the exhaust region has electron density $n_e \approx 5 \times 10^{18} \text{ cm}^{-3}$, electron temperature $T_e \approx 200\text{--}300 \text{ eV}$, mean ion charge $Z \approx 18$ and flow velocity $v \approx 1.5\text{--}3.5 \times 10^5 \text{ m s}^{-1}$, which roughly matches the Alfvén speed ($1.2\text{--}2.0 \times 10^5 \text{ m s}^{-1}$).

Ion and electron acoustic bursts and electron heating

Thomson scattering from IAWs reveals that current-driven instabilities develop at 7 ns. The narrowband spectrometer captured the asymmetric (10:1) IAW Stokes and anti-Stokes peaks. The scattering signals grow from the thermal level by three orders of magnitude to extremely intense, bursty and asymmetric (~ 100 :1) IAW peaks during 7–8 ns. This is shown in Fig. 2a, as a sign of the ion turbulence induced by an unstable IAW⁵¹. The asymmetry in the IAW Stokes and anti-Stokes peaks is the feature of the drift between electrons and ions, which differs the electron Landau damping rates for IAWs in the two directions^{52,59}. As shown in Fig. 2c, the Thomson scattering spectrum lineout before the IAW bursts (Fig. 2a, dashed line) can be reproduced in the synthetic spectrum (Fig. 2c, green dashed line) when electrons ($n_e = 5 \times 10^{18} \text{ cm}^{-3}$, $T_e = 200 \text{ eV}$) are drifting with $v_d = 0.17\sqrt{T_e/m_e}$ relative to ions ($T_i = 400 \text{ eV}$, $Z = 18$). This electron outflow speed is $-5v_A$ and $-0.06v_{Ae}$.

The IAW resonant peak is broader than the synthetic spectrum, assuming that the flow velocity is uniform in the scattering volume, but the broader peak can be reproduced by including the inhomogeneity of the flow velocity with $\Delta v = 2 \times 10^4 \text{ m s}^{-1}$, which may be induced by a spatial gradient of the flow velocity or turbulence. The synthetic spectrum calculation assumes that the resonant wave is stable and the density fluctuations are at the thermal level. The scattering signals are at the thermal level at the initial stage before the IAW bursts. However, based on the electrostatic dispersion equation,

$$1 - \frac{\omega_{pe}^2}{2k^2 T_e/m_e} Z' \left(\frac{\omega/k - v_d}{\sqrt{2T_e/m_e}} \right) - \frac{\omega_{pi}^2}{2k^2 T_i/m_i} Z' \left(\frac{\omega/k}{\sqrt{2T_i/m_i}} \right) = 0, \quad (1)$$

where Z' is the derivative of the plasma dispersion function⁶⁰, the plasma with such strong electron drift is unstable to the IAW, and the maximum growth rate is 17 ns^{-1} ($1.4 \times 10^{-4} \omega_{pe}$ and $0.058 \text{ ns } e\text{-folding time}$) at $k = 0.33/\lambda_{De}$ ($\lambda_{De} = \sqrt{T_e/m_e}/\omega_{pe}$). The wavelength is six times shorter than the electrons' mean free path, which suggests that collisions are unimportant for IAW growth. This theoretical IAW growth rate agrees with the exponential growth of the scattering signal, which is proportional to the square of the density fluctuation $\delta n_e^2(\omega, \mathbf{k})$. As shown in Fig. 3b, during the growth of the first spike, the IAW signal rises exponentially with $0.025 \text{ ns } e\text{-folding time}$ or $3.3 \times 10^{-4} \omega_{pe}$ growth rate, which is almost two times the calculated IAW growth rate. The agreement between the density fluctuation (scattering signal) growth rate and calculated IAW growth rate also confirmed the electron drift speed. In addition, the peak intensity of the IAW scattering is three

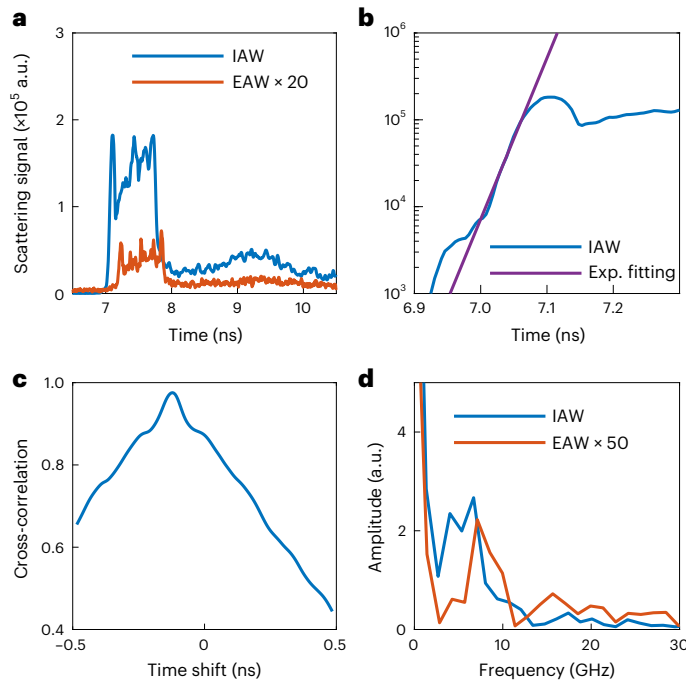


Fig. 3 | Time evolution of IAW and EAW signals. **a**, IAW and EAW Thomson scattering signals in the dashed (IAW) and dash-dotted (EAW) regions in Fig. 2b. Bursts of IAWs and EAWs are shown at around 7–8 ns. **b**, Zoomed-in plot of **a** in the \log_{10} scale to show the growth phase of the IAW signal, which is fitted by an exponential function with e -folding time of 0.025 ns ($3,200\omega_{pe}^{-1}$), agreeing with the IAW growth rate, that is, $\gamma \approx 1.4 \times 10^{-4}\omega_{pe}$, where ω_{pe} is the electron plasma frequency. **c**, Cross-correlation of the IAW and EAW signal shows a strong correlation between the IAW and EAW. The IAW leads the EAW by 0.12 ns $\approx 1.5 \times 10^4\omega_{pe}^{-1}$. **d**, Fourier transform of the 7–8 ns signal shows that both IAW and EAW signals are oscillating with an amplitude peak frequency at 7 GHz. This frequency matches the lower hybrid frequency in a 20 T magnetic field.

orders of magnitude higher than that when no burst presents near 5 ns, indicating that the fluctuation amplitude ($\delta n_e(\omega, \mathbf{k})$ at $k = 2\pi/527 \text{ nm}^{-1}$) is ~ 30 times higher than the thermal level.

With about 0.12 ns delay from IAW bursts (Fig. 3c), a scattering peak appears with an $\sim 13 \text{ nm}$ redshifted wavelength (Fig. 2b), corresponding to a phase velocity of $0.025c \approx 1.2\sqrt{T_e/m_e}$, which is close to the electron thermal speed and matches the EAW's phase velocity. The EAW scattering peaks are also observed in the earlier stage of the reconnection (Fig. 4). The appearance of the EAW scattering peak requires a non-Maxwellian velocity distribution with a flat or positive slope near the thermal speed to avoid Landau damping or stimulate waves. The red solid line (Fig. 2d, inset) shows the two-stream distribution that produces the synthetic spectrum with a strong EAW peak (red solid line). The velocity at the valley of the distribution matches the phase velocity of the EAW peak. The spectrum may allow other distributions to fit. Here we choose a two-stream distribution to reduce the complexity of the distribution function.

The amplitude of the IAWs and EAWs during the bursty period (7–8 ns) is shown to be modulated at a frequency of $\sim 7 \text{ GHz}$ (Fig. 3d), close to the lower hybrid frequency ($\sqrt{f_{ce}f_{ci}}$) at $B = 20 \text{ T}$. One candidate to explain such observations is the modified two-stream instability^{20,28} driven by the electron outflow jet perpendicular to the local magnetic field in the exhaust region. The modified two-stream instability can generate electric-field fluctuations nearly parallel to the current, which may modulate the IAW as well as the generation of EAW bursts. Waves near the lower hybrid frequency were often observed in the magnetospheric multiscale (MMS) mission⁶¹ and the magnetic reconnection experiment²⁰, and have been suggested to mediate energy dissipation. This modulation near the lower hybrid frequency suggests instabilities

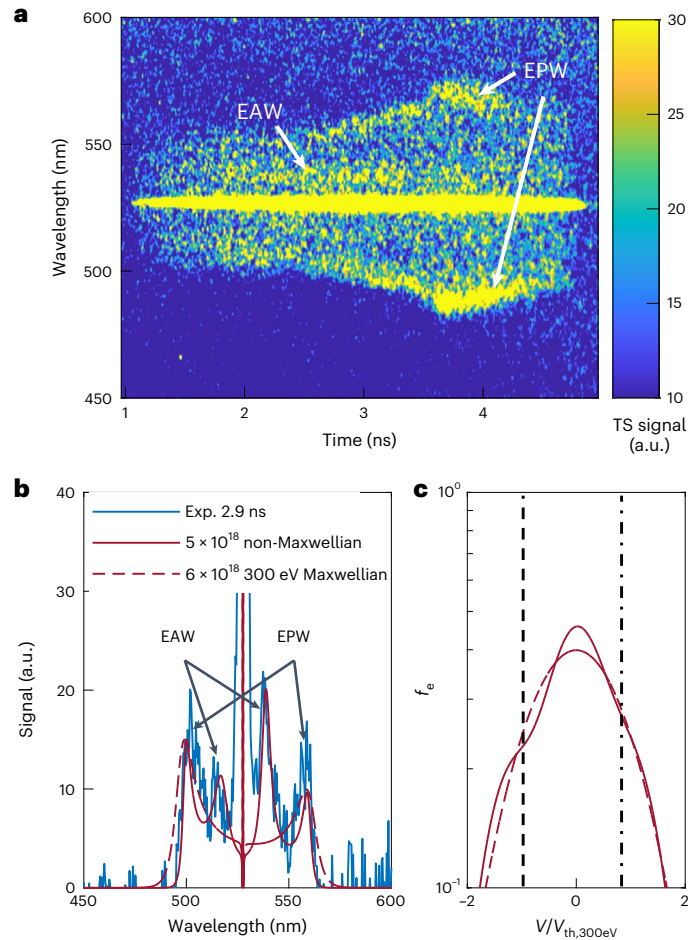


Fig. 4 | Thomson scattering data for EPWs and EAWs in the early stage. **a**, Time-resolved Thomson scattering (TS) shows the features of EPWs and EAWs. The onset of UV lasers is at 0 ns. **b**, Comparison between the measured TS spectrum at $t = 2.9 \text{ ns}$ and the synthetic TS spectra with Maxwellian electrons (electron temperature $T_e = 300 \text{ eV}$, dashed line) versus non-Maxwellian electrons (solid line). **c**, Velocity distribution functions f_e . The non-Maxwellian distribution (solid line) is constructed with secondary components ($n_e = 1.15 \times 10^{18} \text{ cm}^{-3}$, $T_e = 75 \text{ eV}$) counter-streaming with $-1.2v_{th,300\text{eV}}$ and $+1.1v_{th,300\text{eV}}$ relative to a steady component ($n_e = 2.7 \times 10^{18} \text{ cm}^{-3}$, $T_e = 75 \text{ eV}$). Here v_{th} is the electron thermal velocity and $v_{th,300\text{eV}}$ is the velocity when the temperature is at 300 eV. The $-v$ direction is along the redshifted \mathbf{k} (Fig. 1b). This non-Maxwellian distribution with counter-streaming secondary components is required to match the measured spectrum since it avoids Landau damping near the EAW phase velocities by reducing the velocity slope. The EAW phase velocities are marked with a dashed line corresponding to the EAW at 539 nm and a dash-dotted line for the EAW at 517 nm.

like modified two-stream instability may affect the electron outflow, but further study is needed to characterize the role of this lower hybrid modulation.

Electron heating is also captured since the electron temperature increases by 60% during IAW and EAW bursts. Electron temperature is measured from the separation between the IAW's Stokes and anti-Stokes peaks, which is proportional to the ion acoustic velocity as $\Delta\omega \approx 2k\sqrt{ZT_e/m_i}$. Compared with the wavelength separation between IAW peaks before the wave bursts (7.0 ns), this separation is 25% larger after the IAW and EAW bursts (8.5 ns).

One-dimensional local PIC simulation

To understand the bursts of the correlated IAWs and EAWs, we have used a 1D electrostatic PIC code⁶² to simulate the thermal electrons (initial electron temperature $T_{e0} = 320 \text{ eV}$) drifting relative to ions with a velocity $v_d = 0.5\sqrt{T_{e0}/m_e}$, which is higher than the measured drift

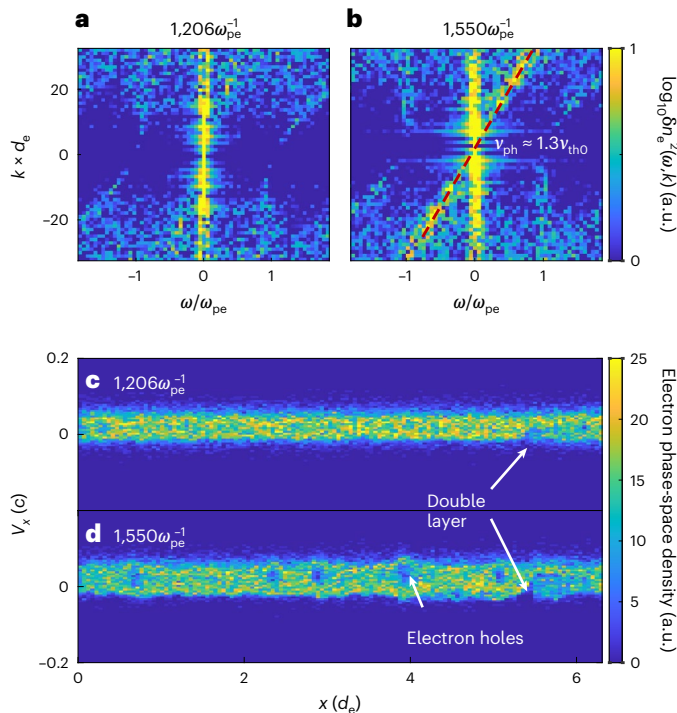


Fig. 5 | Reproduction of IAW and EAW by 1D PIC simulation. a, b, Electron density dispersion plots before ($t = 1,206\omega_{pe}^{-1}$) and during the EAW bursts ($t = 1,550\omega_{pe}^{-1}$), where ω_{pe} is the electron plasma frequency. Wavenumber k is normalized by $1/d_e$ (electron skin depth $d_e = c/\omega_{pe}$). The red dashed line is the dispersion relation with phase velocity $v_{ph} = 1.3\sqrt{T_e/m_e}$, where T_e is the electron temperature and m_e is the electron mass. **c, d,** Electron densities in the $x-v_x$ phase space at the times shown in **a** (**c**) and **b** (**d**). The double layer starts to form at $t = 1,206\omega_{pe}^{-1}$ in **c**. After forming the double layer at $t = 1,550\omega_{pe}^{-1}$ in **d**, the electron holes are generated due to the two-stream instabilities downstream of the double layer. These electron holes are moving in the $+x$ direction with a velocity of $1.3\sqrt{T_e/m_e}$, forming the EAW bursts shown in **b**.

speed ($\sim 0.17\sqrt{T_e/m_e}$) to accelerate the process. In this simulation, the drifting electrons induce an ion acoustic instability and generate a double layer at $x \approx 5d_e$. This process agrees with the previous PIC⁶³ and Vlasov simulations⁶⁴.

The IAW and EAW bursts are reproduced in the 1D PIC simulation (Fig. 5). The dispersion plot (Fig. 5b) shows that the EAW burst has a phase velocity of $\sim 1.3\sqrt{T_e/m_e}$ with a broadband frequency of $\sim 0.1-1.0\omega_{pe}$. This phase velocity roughly agrees with the experimentally observed EAW phase velocity ($\sim 1.2\sqrt{T_e/m_e}$). This EAW corresponds to the phase-space holes shown in Fig. 5d, since the holes are centred at almost $\sqrt{T_e/m_e}$ and move forward with that speed. These electron holes originate from the electron two-stream instability downstream of the double layer. This double layer reflects low-energy electrons and accelerates high-energy electrons that can overcome the potential well, resulting in a two-stream distribution, which has been discussed in previous Vlasov simulations⁶⁴. Their simulation also shows that with a realistic mass ratio, the double layer occurs $\sim 10^4\omega_{pe}^{-1}$ after the peak of the IAW fluctuations. The delay between the IAW peak and double-layer generation is consistent with the observed $0.12\text{ ns} \approx 1.5 \times 10^4\omega_{pe}^{-1}$ delay between the IAW and EAW bursts.

Two-dimensional global PIC simulation

In addition to the 1D local PIC simulation showing the unstable IAW-generated double layer and EAWs, our 2D PIC reconnection simulation also confirms the double-layer generation in the outflow region when cold background plasma is present. In the 2D reconnection simulation with cold background plasma, double layers in the outflow region

are developed and create non-Maxwellian and broadened distributions in the double layer downstream. Figure 6a shows the in-plane current map and magnetic-field lines in the entire simulation domain. The double layers are presented by the ion density cavities in the outflow region (Fig. 6b, red circles). These density cavities can present double layers because the cavities coexist with the ion phase-space holes in this simulation, consistent with the Vlasov simulation⁶⁴. The electron phase-space density profile crossing the double layers at $z = -74d_e$ is plotted in Fig. 6c. As shown in the phase-space density profile, upstream of the double layers, the electrons are drifting relative to the ions, which can destabilize the IAW forming the double layers. In the downstream region, the distribution is broadened and shows a non-Maxwellian distribution with double peaks. Besides the current-driven unstable IAW, ion-ion acoustic instability⁶⁵ is also shown in the region with two-streaming ions ($x \approx 500d_e$; Fig. 6b), especially in the 100 and 400 mass ratio cases. However, this ion-ion acoustic instability only creates strong density perturbations; no non-Maxwellian distribution is seen in the electron phase space. Meanwhile, the double layers and downstream non-Maxwellian distribution are persistent with different mass ratios. The observation of the current-driven double layers and the induced non-Maxwellian distribution confirm that with cold background plasmas, the current-driven IAW bursts can result in energy dissipation in the outflow region. The amount of magnetic energy dissipated through this channel may depend on the plasma conditions such as ZT_e/T_i , m_i/m_e , plasma β , electron β_e and system size, which requires further comprehensive studies.

Discussion and outlook

In summary, our low- β magnetic reconnection experiments using laser-driven capacitor coils exhibit current-driven IAW bursts, followed by EAW bursts with electron heating in the exhaust region.

The location and wave direction are consistent with the IAWs observed by the MMS mission⁶⁶, Time History of Events and Macro-scale Interactions during Substorms mission⁶⁷ and Parker Solar Probe mission⁶⁸ when a population of cold ions exists in the background, and their Landau damping is ineffective. The MMS mission observed IAWs in the outflow region with wavevectors in the direction along the magnetic-field lines⁶⁶, consistent with our observations. The Parker Solar Probe mission observed that the triggered IAWs coincide with the core electron heating⁶⁸. These observations suggest that the current-driven instabilities can lead to a bursty magnetic-field energy release. As our 1D and 2D PIC simulations reveal, this energy dissipation process involves IAW-formed double layers producing two-streaming electrons downstream, which induces the electron two-stream instability. This rapidly heats the electrons, braking the electron outflow jet in the ion-diffusion region. Such a double-layer-induced electron two-stream instability may also explain the origin of the EAWs observed by the MMS mission⁶⁹.

This dissipation process in the reconnection exhaust region is confirmed in our experiment; whether this process can occur in the current-sheet region needs further study. A similar mechanism has been observed in the current sheet of a 3D PIC simulation with a strong guide field, in which Buneman instability¹⁶ leads to the formation of double layers and triggers electron two-stream instability¹⁸. In 1D simulations, the Buneman-instability-generated double layer also creates ion and electron phase-space holes^{70,71}. However, without a guide field or with a weak guide field, the electrons would be deflected out of the current sheet within a short period, which is shown in 3D simulations with a finite guide field⁷². The non-steady electron stream in the current sheet may interrupt the growth of instabilities. The growth of IAW and double layer needs $\sim 10^3-10^4\omega_{pe}^{-1}$, as suggested by our experiment. In addition to the time needed, Vlasov simulation and previous particle simulations⁶³ demonstrate that generating the double layer requires a large system size ($>500\lambda_{pe}$). Future experiments and large-scale 3D simulations are needed to study the current-sheet region.

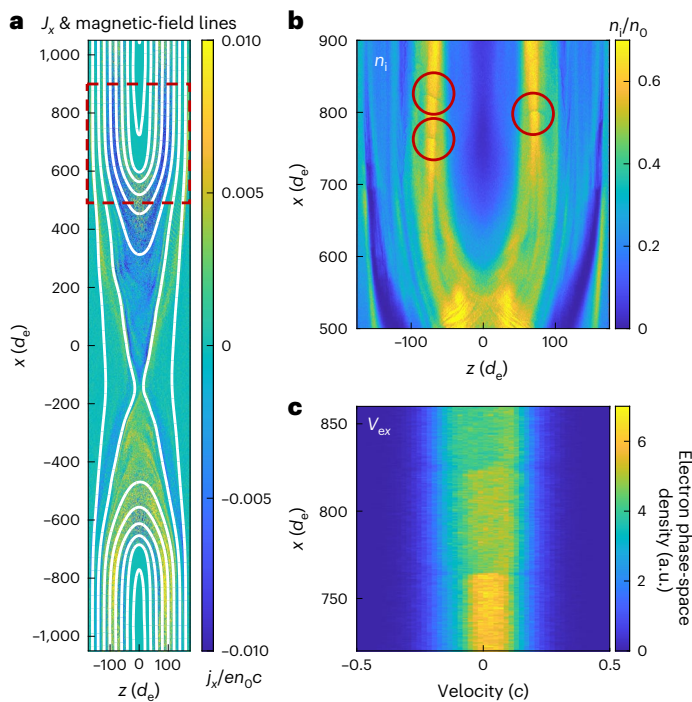


Fig. 6 | Results of the 2D reconnection PIC simulation. The ion/electron mass ratio is $m_i/m_e = 1,600$ and time is $104,000 \omega_{pe}^{-1}$. **a**, Entire profile of the background electron current in the x direction ($J_x = en_{e,bg} v_x$ normalized to $en_0 c$) with magnetic-field lines, where background electrons with density $n_{e,bg}$ have an average velocity in the x direction (v_x). **b**, Cropped region of the background plasma's ion density (n_i , normalized by the peak density of the Harris current sheet n_0) in the outflow region (red dashes in **a**). The double layers, shown as the ion cavities, are circled in red. **c**, Electron density profile in the phase space of the x -direction velocity and x axis (v_{ex} - x) along $z = -74 d_e$ crossing the double layers at $x = 765 d_e$ and $825 d_e$, where $d_e = c/\omega_{pe}$ is the electron skin depth.

The IAW-type turbulence may be important for stellar flares and other plasmas where magnetic reconnection is prevalent, including those of black hole accretion engines. During the initial transient phase of stellar flares, for example, electrons are heated to high temperatures, and ions could remain cold and evade detection⁷³. This condition favours destabilizing IAWs to dissipate current and thus magnetic free energy via electrostatic double layers, in turn triggering EAWs and further heating electrons. Type-III and type-U radio emissions⁷⁴ could be generated by electron beams out of the double-layer structures.

Other low-electron- β two-temperature plasmas, in which the electrons may be much cooler than the ions, may exist in strongly magnetized coronae of black hole accretion discs⁵ or regions within collisionless accretion flows^{6,75}. Here the relative drift between the electrons and ions can be sufficiently large compared with the electron thermal speed to overcome ion Landau damping due to the simultaneous low density and low electron temperature (or equivalently, electron $\beta \ll 1$), and thus, unstable IAWs or the related Buneman instabilities may be viable mechanisms to efficiently dissipate magnetic energy.

In this context, we note that the observed current-driven unstable IAW provides a collisionless coupling of ions and electrons: during the current-driven unstable IAW, the magnetic energy is converted into ion energy in IAWs and eventually forms the double layer that provides an electric potential. The double layer stores both ion kinetic energy and electric potential energy, which is then transferred to the electron kinetic energy by accelerating electrons that pass through the double-layer potential well, and heating electrons by the two-stream instability. In standard two-temperature accretion models used to explain curiously quiescent accretors, the rate of coupling between ions and electrons is assumed to be purely Coulomb collisional coupling or

freely parameterized^{6,75}. In these models, accretion produces low luminosity when the ions acquiring free energy from viscosity are unable to transfer their energy to radiating electrons on an accretion timescale. Whether a collisionless faster-than-Coulomb coupling exists in these contexts has been a long-standing open question because the answer can dramatically affect the paradigm as to why these sources appear so quiescent. As such, it will be important to quantify how the specific mechanism that we have identified scales to the astrophysical contexts in future work.

Online content

Any methods, additional references, Nature Portfolio reporting summaries, source data, extended data, supplementary information, acknowledgements, peer review information; details of author contributions and competing interests; and statements of data and code availability are available at <https://doi.org/10.1038/s41567-023-01972-1>.

References

1. Yamada, M., Kulsrud, R. & Ji, H. Magnetic reconnection. *Rev. Mod. Phys.* **82**, 603–664 (2010).
2. Ji, H. et al. Magnetic reconnection in the era of exascale computing and multiscale experiments. *Nat. Rev. Phys.* **4**, 263–282 (2022).
3. Masuda, S., Kosugi, T., Hara, H., Tsuneta, S. & Ogawara, Y. A loop-top hard X-ray source in a compact solar flare as evidence for magnetic reconnection. *Nature* **371**, 495–497 (1994).
4. Hesse, M. & Cassak, P. Magnetic reconnection in the space sciences: past, present, and future. *J. Geophys. Res. Space Phys.* **125**, e2018JA025935 (2020).
5. Di Matteo, T., Blackman, E. G. & Fabian, A. C. Two-temperature coronae in active galactic nuclei. *Mon. Not. R. Astron. Soc.* **291**, L23–L27 (1997).
6. Yuan, F. & Narayan, R. Hot accretion flows around black holes. *Annu. Rev. Astron. Astrophys.* **52**, 529–588 (2014).
7. Hesse, M., Schindler, K., Birn, J. & Kuznetsova, M. The diffusion region in collisionless magnetic reconnection. *Phys. Plasmas* **6**, 1781–1795 (1999).
8. Kulsrud, R., Ji, H., Fox, W. & Yamada, M. An electromagnetic drift instability in the magnetic reconnection experiment and its importance for magnetic reconnection. *Phys. Plasmas* **12**, 082301 (2005).
9. Burch, J. L. et al. Electron-scale measurements of magnetic reconnection in space. *Science* **352**, aaf2939 (2016).
10. Torbert, R. B. et al. Electron-scale dynamics of the diffusion region during symmetric magnetic reconnection in space. *Science* **362**, 1391–1395 (2018).
11. Ji, H. et al. New insights into dissipation in the electron layer during magnetic reconnection. *Geophys. Res. Lett.* **35**, L13106 (2008).
12. Cozzani, G. et al. Structure of a perturbed magnetic reconnection electron diffusion region in the Earth's magnetotail. *Phys. Rev. Lett.* **127**, 215101 (2021).
13. Lapenta, G., Markidis, S., Divin, A., Newman, D. & Goldman, M. Separatrices: the crux of reconnection. *J. Plasma Phys.* **81**, 325810109 (2015).
14. Kennel, C. & Petschek, H. Limit on stably trapped particle fluxes. *J. Geophys. Res.* **71**, 1–28 (1966).
15. Goldman, M. V. et al. Čerenkov emission of quasiparallel whistlers by fast electron phase-space holes during magnetic reconnection. *Phys. Rev. Lett.* **112**, 145002 (2014).
16. Buneman, O. Instability, turbulence, and conductivity in current-carrying plasma. *Phys. Rev. Lett.* **1**, 8–9 (1958).
17. Drake, J. et al. Formation of electron holes and particle energization during magnetic reconnection. *Science* **299**, 873–877 (2003).

18. Che, H., Drake, J. F., Swisdak, M. & Yoon, P. H. Nonlinear development of streaming instabilities in strongly magnetized plasma. *Phys. Rev. Lett.* **102**, 145004 (2009).
19. Carter, T., Ji, H., Trintchouk, F., Yamada, M. & Kulsrud, R. Measurement of lower-hybrid drift turbulence in a reconnecting current sheet. *Phys. Rev. Lett.* **88**, 015001 (2002).
20. Ji, H. et al. Electromagnetic fluctuation during fast reconnection in a laboratory plasma. *Phys. Rev. Lett.* **92**, 115001 (2004).
21. Ji, H., Kulsrud, R., Fox, W. & Yamada, M. An obliquely propagating electromagnetic drift instability in the lower hybrid frequency range. *J. Geophys. Res.* **110**, A08212 (2005).
22. Fox, W., Porkolab, M., Egedal, J., Katz, N. & Le, A. Laboratory observations of electron energization and associated lower-hybrid and Trivelpiece–Gould wave turbulence during magnetic reconnection. *Phys. Plasmas* **17**, 072303 (2010).
23. Yoo, J. et al. Whistler wave generation by anisotropic tail electrons during asymmetric magnetic reconnection in space and laboratory. *Geophys. Res. Lett.* **45**, 8054–8061 (2018).
24. Graham, D. B. et al. Universality of lower hybrid waves at Earth’s magnetopause. *J. Geophys. Res. Space Phys.* **124**, 8727–8760 (2019).
25. Chen, L.-J. et al. Lower-hybrid drift waves driving electron nongyrotropic heating and vortical flows in a magnetic reconnection layer. *Phys. Rev. Lett.* **125**, 025103 (2020).
26. Yoo, J. et al. Lower hybrid drift waves during guide field reconnection. *Geophys. Res. Lett.* **47**, e2020GL087192 (2020).
27. Krall, N. & Liewer, P. Low-frequency instabilities in magnetic pulses. *Phys. Rev. A* **4**, 2094–2103 (1971).
28. McBride, J. B., Ott, E., Boris, J. P. & Orens, J. H. Theory and simulation of turbulent heating by the modified two-stream instability. *Phys. Fluids* **15**, 2367–2383 (1972).
29. Daughton, W. Two-fluid theory of the drift kink instability. *J. Geophys. Res. Space Phys.* **104**, 28701–28707 (1999).
30. Nakamura, T. et al. Turbulent mass transfer caused by vortex induced reconnection in collisionless magnetospheric plasmas. *Nat. Commun.* **8**, 1582 (2017).
31. Coppi, B. & Friedland, A. B. Processes of magnetic-energy conversion and solar flares. *Astrophys. J.* **169**, 379–404 (1971).
32. Smith, D. F. & Priest, E. Current limitation in solar flares. *Astrophys. J.* **176**, 487–495 (1972).
33. Coroniti, F. & Eviatar, A. Magnetic field reconnection in a collisionless plasma. *Astrophys. J. Suppl. Ser.* **33**, 189–210 (1977).
34. Sagdeev, R. Z. The 1976 Oppenheimer lectures: critical problems in plasma astrophysics. I. Turbulence and nonlinear waves. *Rev. Mod. Phys.* **51**, 1–9 (1979).
35. Ugai, M. & Tsuda, T. Magnetic field-line reconexion by localized enhancement of resistivity: part 1. Evolution in a compressible MHD fluid. *J. Plasma Phys.* **17**, 337–356 (1977).
36. Sato, T. & Hayashi, T. Externally driven magnetic reconnection and a powerful magnetic energy converter. *Phys. Fluids* **22**, 1189–1202 (1979).
37. Aparicio, J., Haines, M. G., Hastie, R. J. & Wainwright, J. P. Fast reconnection due to localized anomalous resistivity. *Phys. Plasmas* **5**, 3180–3186 (1998).
38. Kulsrud, R. M. Magnetic reconnection in a magnetohydrodynamic plasma. *Phys. Plasmas* **5**, 1599–1606 (1998).
39. Kulsrud, R. Magnetic reconnection: Sweet-Parker versus Petschek. *Earth Planet. Sp.* **53**, 417–422 (2001).
40. Uzdensky, D. A. Petschek-like reconnection with current-driven anomalous resistivity and its application to solar flares. *Astrophys. J.* **587**, 450–457 (2003).
41. Gekelman, W. & Stenzel, R. Magnetic field line reconnection experiments: 6. Magnetic turbulence. *J. Geophys. Res. Space Phys.* **89**, 2715–2733 (1984).
42. Chien, A. et al. Non-thermal electron acceleration from magnetically driven reconnection in a laboratory plasma. *Nat. Phys.* **19**, 254–262 (2023).
43. Boehly, T. et al. Initial performance results of the OMEGA laser system. *Opt. Commun.* **133**, 495–506 (1997).
44. Li, C. K. et al. Measuring E and B fields in laser-produced plasmas with monoenergetic proton radiography. *Phys. Rev. Lett.* **97**, 135003 (2006).
45. Gao, L. et al. Ultrafast proton radiography of the magnetic fields generated by a laser-driven coil current. *Phys. Plasmas* **23**, 043106 (2016).
46. Chien, A. et al. Study of a magnetically driven reconnection platform using ultrafast proton radiography. *Phys. Plasmas* **26**, 062113 (2019).
47. Chien, A. et al. Pulse width dependence of magnetic field generation using laser-powered capacitor coils. *Phys. Plasmas* **28**, 052105 (2021).
48. Fryxell, B. et al. FLASH: an adaptive mesh hydrodynamics code for modeling astrophysical thermonuclear flashes. *Astrophys. J. Suppl. Ser.* **131**, 273 (2000).
49. Milder, A. L. et al. Direct measurement of the return current instability in a laser-produced plasma. *Phys. Rev. Lett.* **129**, 115002 (2022).
50. Froula, D. H. et al. Stimulated Brillouin scattering in the saturated regime. *Phys. Plasmas* **10**, 1846–1853 (2003).
51. Daughney, C. C., Holmes, L. S. & Paul, J. W. M. Measurement of spectrum of turbulence within a collisionless shock by collective scattering of light. *Phys. Rev. Lett.* **25**, 497–499 (1970).
52. Froula, D. H., Glenzer, S. H., Luhmann, N. C. J. & Sheffield, J. *Plasma Scattering of Electromagnetic Radiation: Theory and Measurement Techniques* 2nd edn (Elsevier, 2011).
53. Suttle, L. G. et al. Structure of a magnetic flux annihilation layer formed by the collision of supersonic, magnetized plasma flows. *Phys. Rev. Lett.* **116**, 225001 (2016).
54. Hare, J. D. et al. Anomalous heating and plasmoid formation in a driven magnetic reconnection experiment. *Phys. Rev. Lett.* **118**, 085001 (2017).
55. Suttle, L. G. et al. Collective optical Thomson scattering in pulsed-power driven high energy density physics experiments (invited). *Rev. Sci. Instrum.* **92**, 033542 (2021).
56. Sakai, K. et al. Collective Thomson scattering in non-equilibrium laser produced two-stream plasmas. *Phys. Plasmas* **27**, 103104 (2020).
57. Swadling, G. F. et al. Measurement of kinetic-scale current filamentation dynamics and associated magnetic fields in interpenetrating plasmas. *Phys. Rev. Lett.* **124**, 215001 (2020).
58. Milder, A. L. et al. Evolution of the electron distribution function in the presence of inverse bremsstrahlung heating and collisional ionization. *Phys. Rev. Lett.* **124**, 025001 (2020).
59. Hawreliak, J. et al. Thomson scattering measurements of heat flow in a laser-produced plasma. *J. Phys. B: At. Mol. Opt. Phys.* **37**, 1541–1551 (2004).
60. Fried, B. D. & Conte, S. D. *The Plasma Dispersion Function: The Hilbert Transform of the Gaussian* (Academic Press, 1961).
61. Khotyaintsev, Y. V. et al. Electron heating by Debye-scale turbulence in guide-field reconnection. *Phys. Rev. Lett.* **124**, 045101 (2020).
62. Markidis, S. & Lapenta, G. The energy conserving particle-in-cell method. *J. Comput. Phys.* **230**, 7037–7052 (2011).
63. Sato, T. & Okuda, H. Ion-acoustic double layers. *Phys. Rev. Lett.* **44**, 740–743 (1980).
64. Vazsonyi, A. R., Hara, K. & Boyd, I. D. Non-monotonic double layers and electron two-stream instabilities resulting from intermittent ion acoustic wave growth. *Phys. Plasmas* **27**, 112303 (2020).
65. Gary, S. P. & Omid, N. The ion–ion acoustic instability. *J. Plasma Phys.* **37**, 45–61 (1987).

66. Steinvall, K. et al. Large amplitude electrostatic proton plasma frequency waves in the magnetospheric separatrix and outflow regions during magnetic reconnection. *Geophys. Res. Lett.* **48**, e2020GL090286 (2021).
67. Uchino, H., Kurita, S., Harada, Y., Machida, S. & Angelopoulos, V. Waves in the innermost open boundary layer formed by dayside magnetopause reconnection. *J. Geophys. Res. Space Phys.* **122**, 3291–3307 (2017).
68. Mozer, F. S. et al. Core electron heating by triggered ion acoustic waves in the solar wind. *Astrophys. J. Lett.* **927**, L15 (2022).
69. Ergun, R. E. et al. Magnetospheric multiscale observations of large-amplitude, parallel, electrostatic waves associated with magnetic reconnection at the magnetopause. *Geophys. Res. Lett.* **43**, 5626–5634 (2016).
70. Smith, R. A. A review of double layer simulations. *Phys. Scr.* **T2A**, 238–251 (1982).
71. Goldman, M. V., Newman, D. L. & Ergun, R. E. Phase-space holes due to electron and ion beams accelerated by a current-driven potential ramp. *Nonlin. Processes Geophys.* **10**, 37–44 (2003).
72. Daughton, W. et al. Role of electron physics in the development of turbulent magnetic reconnection in collisionless plasmas. *Nat. Phys.* **7**, 539–542 (2011).
73. Polito, V. et al. Broad non-Gaussian Fe xxiv line profiles in the impulsive phase of the 2017 September 10 X8.3-class flare observed by Hinode/EIS. *Astrophys. J.* **864**, 63 (2018).
74. Miteva, R., Mann, G., Vocks, C. & Aurass, H. Excitation of electrostatic fluctuations by jets in a flaring plasma. *Astron. Astrophys.* **461**, 1127–1132 (2007).
75. Narayan, R., Mahadevan, R. & Quataert, E. Advection-dominated accretion around black holes. in *Theory of Black Hole Accretion Disks* (eds Abramowicz, M. A. et al.) 148–182 (Cambridge Univ. Press, 1998).

Publisher's note Springer Nature remains neutral with regard to jurisdictional claims in published maps and institutional affiliations.

Springer Nature or its licensor (e.g. a society or other partner) holds exclusive rights to this article under a publishing agreement with the author(s) or other rightsholder(s); author self-archiving of the accepted manuscript version of this article is solely governed by the terms of such publishing agreement and applicable law.

© The Author(s), under exclusive licence to Springer Nature Limited 2023

Methods

Here we present the setup of the Thomson scattering diagnostics, calculation of the synthetic Thomson scattering spectrum, and the parameters of 1D and 2D PIC simulations. The FLASH radiative non-ideal MHD simulations and the proton radiography used to confirm the existence of reconnection are presented in the Supplementary Information.

Collective Thomson scattering

In this experiment, an $f/10$ reflective collection system 63° off the probe's axis⁷⁶ collects the scattered light from a $60 \times 60 \times 50 \mu\text{m}^3$ volume near the focus. Narrowband (7 nm window) and broadband (320 nm window) streaked spectrometers temporally and spectrally resolve the collected scattering light. The streak window is 5 ns. The narrowband spectrometer covers the light scattered by the IAWs. The broadband spectrometer can show the spectrum of the light scattered by the EAW, EPW and merged IAW peaks. The timing of the probe is changed for each shot to cover the entire reconnection process.

Collective Thomson scattering is used to diagnose the plasma conditions since the spectrum of the scattered light is sensitive to the plasma's density, temperature and velocity⁵². In this experiment, the electron density and temperature are given by least-squares fitting of the synthetic spectrum to the measured spectrum of the EPW resonances (Fig. 4a). With the measured T_e and n_e values, we fit the IAW resonance peaks to diagnose the mean ion charge (Z) and ion temperature T_i , because the separation between the IAW peaks is determined by the IAW's phase velocity ($\sqrt{ZT_e/m_i}$) and the width of the peaks and the peak-to-trough ratio are determined by T_i . The $Z \approx 18$ ion charge also agrees with the FLYCHK⁷⁷ simulation. The shift of the IAW peaks is due to Doppler shift, which gives the flow velocity. The asymmetry of the IAW peaks is used to calibrate the relative drift between the electrons and ions since the drift can induce different electron Landau damping rates on the IAWs in two directions. The plasma is collisionless for Thomson scattering since the electron mean free path is one order of magnitude larger than the probe's wavelength.

To forward fit the measured Thomson scattering spectrum, we calculated the synthetic power spectrum (Figs. 2 and 4) based on the model summarized elsewhere⁵². The synthetic power spectrum for arbitrary velocity distributions is

$$P(\lambda_s) \propto \left(1 + \frac{2\omega}{\omega_0}\right) \left[\frac{2\pi}{k} \left| \frac{1+\chi_i}{1+\chi_e+\chi_i} \right|^2 f_e\left(\frac{\omega}{k}\right) + \frac{2\pi Z}{k} \left| \frac{\chi_e}{1+\chi_e+\chi_i} \right|^2 f_i\left(\frac{\omega}{k}\right) \right] \frac{d\omega}{d\lambda_s}, \quad (2)$$

where $\omega = \omega_s - \omega_0$ is the angular frequency of the fluctuations scattering the probe light (ω_0, \mathbf{k}_0) and generating the scattered light (ω_s, \mathbf{k}_s), and $f_{e,i}(\nu)$ are the electron/ion velocity distributions reduced to one dimension along the \mathbf{k} direction. The electron and ion susceptibilities are given by

$$\chi_{e,i}(\omega, k) = \int_{-\infty}^{\infty} d\nu \frac{\omega_{pe,i}^2}{k^2} \frac{k \partial f_{e,i} / \partial \nu}{\omega - k\nu}. \quad (3)$$

EAW resonance in Thomson scattering

Figure 4a shows the time evolution of the Thomson scattering spectrum from the broadband spectrometer, and the spectrum at 2.9 ns is shown in Fig. 4b (blue line). In addition to the Stokes and anti-Stokes scattering of the EPW usually seen in thermal plasmas, the Thomson scattering spectrum also shows resonant peaks with a lower wavelength shift (~ 10 nm), indicating the non-Maxwellian distribution in the reconnection exhaust. These shorter-wavelength resonant peaks are caused by EAWs with phase velocities near the electron thermal velocity $v_{e,th} = \sqrt{T_e/m_e}$, which would be Landau damped if the electron velocity distribution was Maxwellian (Fig. 4b, red dashed line). To reproduce

the EAW peaks, we modified the distribution function by combining two counter-streaming beams with the steady component to reduce the slope near the thermal speed (Fig. 4c, solid red line). Figure 4b (solid line) shows the fitted scattering spectrum calculated based on equation (2). This three-component distribution is similar to the observed ring-core distribution in reconnection PIC simulations⁷⁸, in which the ring in the outflow out-of-plane (v_x-v_y) phase space reduces to two counter-streaming beams in v_x . This ring structure is probably produced by the reconnected magnetic field (B_y) turning the accelerated electrons⁷⁹. Similar ring-core distribution has also been observed by the MMS mission in the reconnection exhaust region^{9,10}.

One-dimensional PIC simulation

The simulation was performed in a $2\pi c/\omega_{pe}$ ($2\pi d_e$) periodic domain with a reduced ion mass $m_i/m_e = 100$ and a lower ion temperature $T_i = 20$ eV to keep the ion thermal speed lower than the IAW's phase velocity. The simulation domain contains 256 cells and 128 particles per cell. To sustain the electrons streaming in the simulation with limited size, we have added an external electric field $E_x = 10^{-5} m_e c \omega_{pe} / e$ to the electric field calculated by the Poisson equation for advancing the particles' velocity.

Two-dimensional PIC simulation

The 2D PIC simulations use OSIRIS code^{80,81} to simulate a Harris current sheet⁸² and a cold background plasma initialized with a density profile as

$$n_{bg}(z) = 0.3n_0 \left[\frac{1}{2} + \frac{1}{2} \tanh\left(\frac{|z| - 2.0L}{0.5L}\right) \right], \quad (4)$$

where n_0 is the peak density of the Harris current sheet and $L = 20d_e$. This simulation setup is similar to the cold background simulation described elsewhere⁸³. This setup allows a low ion temperature in the outflow region to avoid ion Landau damping for IAWs. The Harris current sheet has hot ions with $T_{i,Harris} = 5T_{e,Harris}$. The background plasma is initialized with $T_{i,bg} = T_{e,bg} = T_{e,Harris}/25$. The anti-parallel magnetic field is in the x direction with $B_x = B_0 \tanh(z/L)$, where $B_0/em_e = \omega_{ce} = 0.5\omega_{pe}$. A long-wavelength perturbation⁸⁴ with 0.01 B_0 amplitude is included to initialize the reconnection. The simulation has a $2,100d_e \times 350d_e$ box size in $6,144 \times 1,024$ cells. The boundaries are periodic in the x direction. The z -direction boundaries are reflective for particles and conductive for the electric field. The mass ratio has been scanned for $m_i/m_e = 100, 400$ and $1,600$.

Data availability

The experimental Thomson scattering spectrograms are available on request from the corresponding authors.

Code availability

The synthetic Thomson scattering calculation code is available on request from the corresponding authors. The 1D electrostatic PIC simulation code is available in ref. ⁶². The OSIRIS 4.0 PIC simulation code is available to authorized users by signing memoranda of understanding with the OSIRIS Consortium, consisting of IST and UCLA. FLASH rad-MHD code is available at <https://flash.rochester.edu>. The calculation code for the plasma dispersion relation is available in the PlasmaDispersionRelation repository via GitHub at <https://github.com/xiaoshulittletree>.

References

76. Katz, J. et al. A reflective optical transport system for ultraviolet Thomson scattering from electron plasma waves on OMEGA. *Rev. Sci. Instrum.* **83**, 10E349 (2012).
77. Chung, H.-K., Chen, M., Morgan, W., Ralchenko, Y. & Lee, R. FLYCHK: generalized population kinetics and spectral model for rapid spectroscopic analysis for all elements. *High Energ. Dens. Phys.* **1**, 3–12 (2005).

78. Shuster, J. R. et al. Highly structured electron anisotropy in collisionless reconnection exhausts. *Geophys. Res. Lett.* **41**, 5389–5395 (2014).
79. Bessho, N., Chen, L.-J., Shuster, J. R. & Wang, S. Electron distribution functions in the electron diffusion region of magnetic reconnection: physics behind the fine structures. *Geophys. Res. Lett.* **41**, 8688–8695 (2014).
80. Fonseca, R. A. et al. OSIRIS: a three-dimensional, fully relativistic particle in cell code for modeling plasma based accelerators. In *Computational Science—ICCS 2002* (eds Sloot, P. M. A. et al.) 342–351 (Springer, 2002).
81. Hemker, R. G. *Particle-in-Cell Modeling of Plasma-Based Accelerators in Two and Three Dimensions* (Univ. of California, Los Angeles, 2000).
82. Harris, E. On a plasma sheath separating regions of oppositely directed magnetic field. *Nuovo Cim.* **23**, 115–121 (1962).
83. Norgren, C. et al. On the presence and thermalization of cold ions in the exhaust of antiparallel symmetric reconnection. *Front. Astron. Space Sci.* **8**, 730061 (2021).
84. Birn, J. et al. Geomagnetic environmental modeling (GEM) magnetic reconnection challenge. *J. Geophys. Res.* **106**, 3715–3719 (2001).

Acknowledgements

This research is supported by the US Department of Energy (DoE), Office of Science, Office of Fusion Energy Sciences High-Energy-Density Laboratory Plasma Science program, under award no. DE-SC0020103 (H.J., S.Z., A.C., L.G. and E.G.B.). The experiment was conducted at the OMEGA Laser Facility at the University of Rochester's Laboratory for Laser Energetics with the beam time through the National Laser Users' Facility (NLUF) Program supported by DoE/National Nuclear Security Administration (NNSA). E.G.B. acknowledges support from DoE grants DE-SC0020432 and DE-SC0020434, and NSF grants AST-1813298 and PHY-2020249. J.K., C.L., A.B. and R.P. are supported under the auspices of the US DoE/NNSA (contract DE-NA0003868). The FLASH code used in this work was in part developed by the DoE NNSA-ASC OASCR Flash Center

at the University of Chicago. We would like to acknowledge the OSIRIS Consortium, consisting of UCLA and IST (Lisbon, Portugal), for providing access to the OSIRIS 4.0 framework supported by NSF ACI-1339893. We would like to thank Q. Wang, L. Suttle, J. Halliday, S. Lebedev and W. Daughton for fruitful discussions.

Author contributions

H.J., L.G. and E.G.B. initiated the research. S.Z., A.C., L.G., H.J. and E.G.B. designed the experiment with inputs from J.M., H.C., R.F., D.H.F. and J.K. S.Z., R.F., D.H.F. and J.K. analysed the Thomson scattering spectra. S.Z., A.C., L.G., H.J., J.K., C.L., A.B. and H.C. performed the experiments. C.L., A.B. and R.P. conducted and analysed the proton radiography. H.J. and E.G.B. contributed to the astrophysics implications. S.Z. performed the 1D and 2D PIC simulations, FLASH simulations, synthetic Thomson scattering simulations and synthetic proton radiography simulations. S.Z., A.C., L.G., H.J. and E.G.B. contributed to the simulation data interpretations. S.Z., H.J., E.G.B. and L.G. wrote the manuscript. All the authors read, revised and approved the final version of the manuscript.

Competing interests

The authors declare no competing interests.

Additional information

Supplementary information The online version contains supplementary material available at <https://doi.org/10.1038/s41567-023-01972-1>.

Correspondence and requests for materials should be addressed to Shu Zhang or Hantao Ji.

Peer review information *Nature Physics* thanks Richard Sydora, Yuri Khotyaintsev and the other, anonymous, reviewer(s) for their contribution to the peer review of this work.

Reprints and permissions information is available at www.nature.com/reprints.